Supporting Information

Interfacial Engineering of Ru-RuSb$_2$ for Enhanced Activity and Stability Towards Alkaline Hydrogen Oxidation Reaction

Chaoyi Yang†, Zihao Dai†, Jianchao Yue and Wei Luo*

Experimental Procedures

Reagents and materials

Ruthenium trichloride [$RuCl_3$, ~98%, Wuhan, Changcheng Chemical Co., Ltd.], Antimony trichloride [$SbCl_3$, ~98%, China, Aladdin Industrial Co., Ltd], Ammonium bicarbonate [NH_4HCO_3, >99.99%, China, Aladdin Industrial Co., Ltd], Trisodium citrate dihydrate [$C_6H_5Na_3O_7 \cdot 2H_2O$, >99.99%, China, Sinopharm Chemical Reagent Co., Ltd], Urea [CH_4N_2O, >99.99%, China, Sinopharm Chemical Reagent Co., Ltd], Hydrochloric acid [HCl, 98%, China, Sinopharm Chemical Reagent Co., Ltd], ethanol and isopropanol [>99% and ~99.5%, China, Sinopharm Chemical Reagent Co., Ltd.], nafion solution [5%, Sigma-Aldrich].The water used in all experiments was prepared by passing through an ultra-pure purification system.

Synthesis of Nitrogen-doped porous carbon (NC)

In a typical synthesis of NC, 2.85 g trisodium citrate dihydrat and 250 mg urea were ground and mixed, then annealed at 750 °C for 1 h with ramping temperature at 4 °C min^{-1} in N_2. Then, the obtained sample was washed with 0.1 M hydrochloric acid, washed three times with ultrapure water, and dried to obtain NC.

Synthesis of Ru/NC

In a typical synthesis of Ru/NC, 50 mg NC were dispersed with 40 mL H_2O/ethanol (volume ratio at 1:1). Then 25 mg $RuCl_3$ was added into above mixture and stirring. After 30 min, 250 mg of NH_4HCO_3 was added and the mixture was stirred for 5 h. The black solid was acquired by centrifugation, washing and drying. Finally, Ru/NC was obtained by annealing black solid at 400°C for 2 h with ramping temperature at 5 °C min^{-1} in H_2/N_2.

Synthesis of Ru-RuSb$_2$/NC, RuSb$_2$/NC

In a typical synthesis of Ru-RuSb$_2$/NC, 12.5 mg Ru/NC was mixed in 10 mL ethanol. After ultrasonic dispersion for 30 min, 1.6 mL $SbCl_3$/ethanol (0.028 mol L^{-1}) suspension was added. Ultrasonic treatment of the mixed solution for 30 mins followed by rotary evaporation and drying. Finally, the dried powder was transferred to a tubular furnace and annealed at 600 °C for 1 h with ramping temperature at 5 °C min^{-1} in H_2/N_2. The temperature of the tubular furnace was naturally cooled to room temperature, the samples were collected and named it as Ru-RuSb$_2$/NC. In addition to adjusting the 2.2 mL $SbCl_3$/ethanol (0.028 mol L^{-1}), the preparation steps for RuSb$_2$/NC can remain the same as in other processes.

Physical characterizations

The X-ray powder diffraction (XRD) patterns were obtained on a Rigaku Miniflex600 Xray powder diffractometer equipped with a Cu Kα radiation source (λ = 0.154178 nm) The transmission electron microscopy (TEM) images were performed with JEM-2100 Plus. Scanning transmission electron microscopy (STEM) imaging and energy-dispersive X-ray spectroscopy (EDX) mapping were acquired on a JEOL JEM-ARM200CF microscope operated at 200kV with a Schottky cold-field emission gun. X-ray photoelectron spectroscopy experiments were collected with Thermo Fisher ESCALAB 250Xi using Al Kα radiation source. Inductively coupled plasma atomic emission spectroscopy (ICP-AES) were conducted on a Thermo IRIS Intrepid II XSP atomic emission spectrometer. In situ surface-enhanced infrared absorption spectroscopy (SEIRAS) was carried out with Bruker Invenio R equipped with a liquid nitrogen-cooled detector. A homemade IR cell with a polished Si prism was employed as experimental apparatus.

Electrochemical measurements

All the electrochemical measurements were conducted by the CHI 760E electrochemical analyzer (CH Instruments, Chenhua Co., Shanghai, China). The standard three-electrode-system were adopted. Glass carbon electrode (GCE, diameter: 5 mm) with catalysts coating were used as the working electrode. The Hg/HgO electrode (MOE) (in 0.1 M KOH) and the graphite rod were served as reference electrode in alkaline electrolytes and the counter electrode, respectively. All measured potentials were reported versus the reversible hydrogen electrode (RHE) potential.

To prepare catalyst ink for HOR experiments, 4 mg catalysts were dispersing in 2 ml isopropanol solution containing 0.05% Nafion. The mixture solvent was ultrasonicated for 1h to form homogeneous solution. Then, 5 μL ink was pipetted onto the surface of glassy carbon electrode (GCE, 5 mm in diameter) resulting in a total mass loading of ~ 0.05 mg $cm^{-2}{}_{geo}$. The accurate loading of catalysts and elements contents were originated from the ICP-AES results listing in table S1.

Cyclic voltammetry (CV) was conducted in 0.1 M KOH solution with Ar-saturated at a scanning rate of 50 mV s^{-1} from -0.18 V to 0.72 V. The HOR polarization curves were recorded by a rotation disk electrode (RDE) with a rotation speed of 1600 rpm in a H_2-saturated 0.1 M KOH and the potential range is from -0.08 V to 0.72 V at a scanning rate of 10 mV s^{-1}.

Exchange current density (j^0) obtained from linear fitting of micropolarization regions (−5 to 5 mV), through the simplified Bulter–Volmer equation (Eq. S1)[1]:

$$j^0 = j\frac{RT}{\eta F} \qquad \text{…………Eq. S1}$$

Where R equals the universal gas constant T equals the temperature in the Kelvin scale, F equals Faraday's constant, j equals the measured current density, and η equals the applied overpotential.

The HOR polarization under the rotation speed of 2500, 2025, 1600, 1225, 900, 625 and 400 rpm were collected at a scanning rate of 10 mV s^{-1}. The kinetic current density (j^k) of each electrocatalyst could be calculated from the Koutecky-Levich equation (Eq. S2) [2]

$$\frac{1}{j}=\frac{1}{j^k}+\frac{1}{j^d}=\frac{1}{j^k}+\frac{1}{Bc_0\omega^{1/2}}$$ …………Eq. S2

where j and j^d are the measured and diffusion limited current density, and B represents the Levich constant, c_0 represents the solubility of H_2 (7.33×10^{-4} mol L^{-1}), ω is the rotating speed. Among them, B could be obtained from Eq. S3

$$B = 0.2nFD^{2/3}v^{-1/6}$$ ………… Eq. S3

where n is the numbers of electron transferred, F is the Faraday constant (96485 C mol^{-1}), D is the diffusivity of H_2 (3.7×10^{-5} cm^2 s^{-1}), and v represents the kinematic viscosity (1.01×10^{-2} cm^2 s^{-1}). [3]

Exchange current density (j^0) could be deduced from the Butler–Volmer equation in Eq. S4,

$$j^k = j^0[e^{\frac{\alpha F}{RT}\eta} - e^{\frac{-(1-\alpha)F}{RT}\eta}]$$ …………Eq. S4

where α is the transfer coefficient, R represents the universal gas constant (8.314 J mol^{-1} K^{-1}), T stands the operating temperature (303.15 K), η is the overpotential. [4]

For Ru-based catalysts, the hydrogen underpotential deposition (H-UPD) method is unsuitable for confirming the electrochemically active surface areas (ECSAs) owing to the adsorption of OH* in H-UPD area. [5] Correspondingly, the Cu-UPD method is employed to determine the ECSA for the catalysts. The catalysts modified electrode were cycled between 0.20 and 0.70 V in Ar-saturated solution of 0.1 M H_2SO_4 with 2 mM $CuSO_4$ to obtain a complete CV containing the UPD and overpotential deposition (OPD) of Cu. Since the stripping peaks of Cu-UPD and Cu-OPD are recorded separately, after eliminated the effect of Cu-OPD in the manner of performing the CV from 0.25 V, the region of Cu-UPD is used to calculate the ECSA. Before the deposition fo Cu, the modified electrodes were cycled between 0 and 0.70 V in pure 0.1 M H_2SO_4 as the background. The surface charge density of 420 μC cm^{-2} is assigned as a monolayer adsorption of Cu on catalysts. All the values of ECSAs are exhibited in Table S2. The value of ECSAs could be calculated via Eq. S5:

$$ECSA\left(\frac{cm_{metal}^2}{g_{metal}}\right)=\frac{Q_{Cu}}{M_{metal}\,420C\ cm^{-2}}$$ …………Eq. S5

where M_{metal} is the mass loading of metals on the electrode.

For the CO stripping experiments, the samples were kept at 0.1 V versus RHE for 10 min in the saturated CO to adsorb CO on the metal surface, [6] followed by pumping Ar for 20 min to remove residual CO in the electrolyte. The CO stripping current was collected through cyclic voltammetry in a potential range from 0 to 0.9 V at a scanning rate of 5 mV s^{-1}.

The stability of catalyst was appraised by the accelerated durability tests by scanning the potential between -0.08 and 0.72 V for 1000 cycles at the scanning rate of 500 mV s^{-1}. Then, the HOR polarization curve was recorded in H_2-saturated 0.1 M KOH electrolyte at 10 mV s^{-1} from 0.92 to -0.08 V via the comparison with the initial curve. The loading of catalyst is around 30 μg cm_{disc}^{-2}.

In this work, all the potentials in HOR and HER tests were referred to reversible hydrogen electrode (RHE) with iR-compensation. The uncompensated resistance (R_u) was measured by the electrochemical impedance spectra (EIS) tests. EIS tests were measured from 200 kHz to 0.1 kHz at a voltage perturbation of 5 mV after each RDE measurement. The iR-free potential ($E_{iR\text{-}free}$) was obtained by using the value of the real part of the resistance at 1 kHz, according to the following equation, Eq. S6,

$$E_{iR-free} = E - iR_u \qquad \text{Eq. S6}$$

where E, i are the measured potential and the corresponding current.

Computational methods

Density functional theory (DFT) with the Perdew-Burke-Ernzerhof (PBE) and generalized gradient corrected approximation (GGA) was carried out for electronic structure calculations. [7-8] The cutoff energy was 400 eV and the self-consistent field (SCF) tolerance was 1×10^{-5} eV. The Brillouin zone was sampled by the Monkhorst-Pack scheme with a 4×4×1 k-points mesh for all of the surfaces. All the model with 4*4 supercell and a vacuum width of 10 Å was added in the z axis. For all the optimization calculations, the bottom two layers were fixed while the topmost two layers and the adsorbates were allowed to relax. The binding energies of H* were determined by the following formula $\Delta E_{H^*} = E(\text{surf + H}) - E(\text{surf}) - 1/2E(H_2)$. The binding energies of OH* were determined by the following formula $\Delta E_{OH^*} = E(\text{surf + OH}) - E(\text{surf}) - E(H_2O) + 1/2E(H_2)$.

$E_{sub\text{-}H}$ and $E_{sub\text{-}OH}$ represent total energies of the model with hydrogen and hydroxyl adsorption. E_{sub} represents total energy of the model. E_{H2} and E_{H2O} represent the energy of molecular H_2 and H_2O in gas phase.

The Gibbs free energy of H* adsorption was calculated as follows:

$\Delta G_{H^*} = \Delta E_{H^*} + \Delta ZPE - T\Delta S$

ΔZPE and ΔS represent the zero point energy correction and entropy change of hydrogen adsorption, respectively. And We refer to the previous work for the related values. [9]

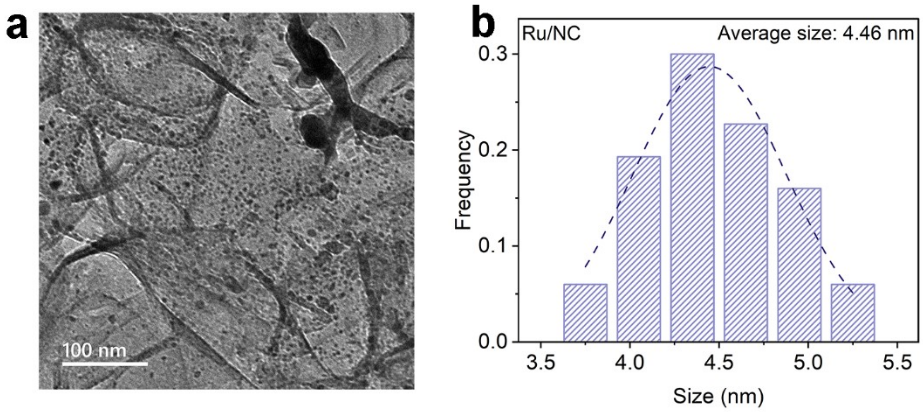

Figure S1 The TEM images of Ru/NC (a) and the corresponding size distribution of (b).

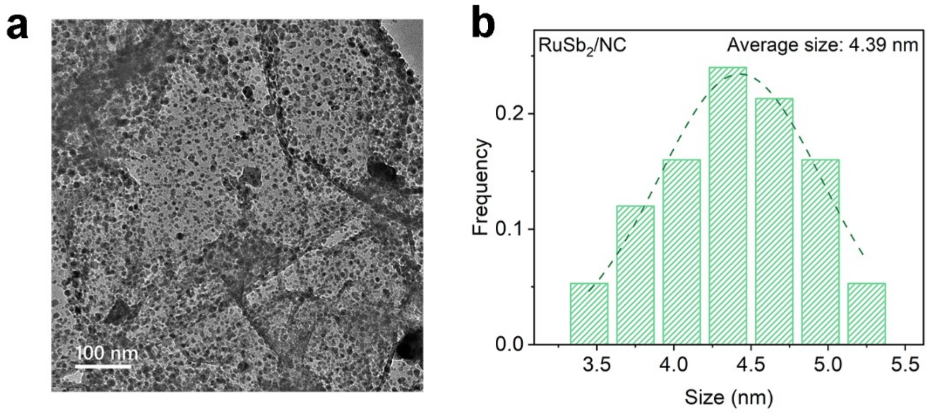

Figure S2 The TEM images of $RuSb_2$/NC (a) and the corresponding size distribution of (b).

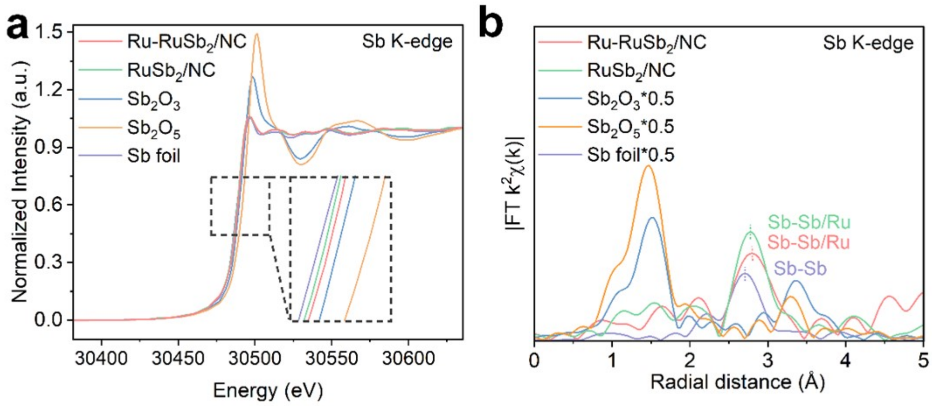

Figure S3 Sb K-edge XANES spectra (a) and corresponding FT-EXAFS spectrum spectra (b) of Ru-$RuSb_2$/NC and $RuSb_2$/NC with the reference of Sb foil, Sb_2O_3 and Sb_2O_5.

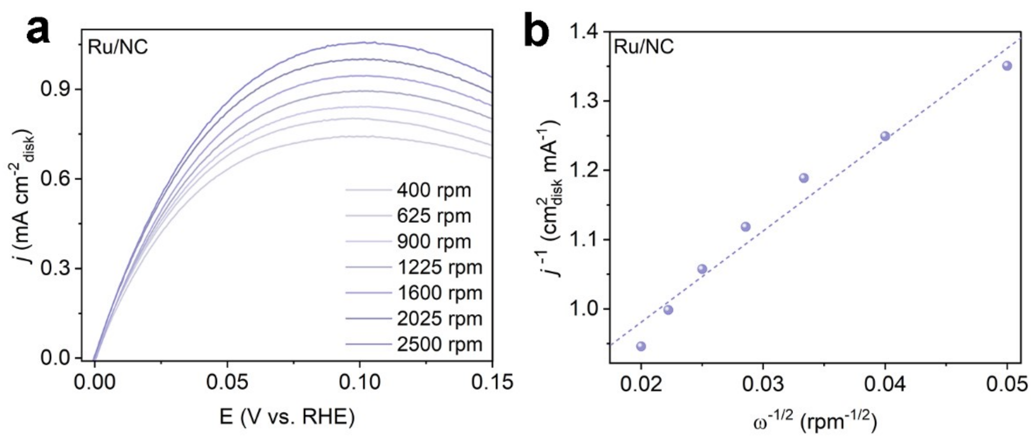

Figure S4 (a) Polarization curves of Ru/NC in H_2-saturated 0.1 M KOH solution at the rotating speeds varied from 2500 to 400 rpm. (b) And the corresponding Koutecky–Levich plot.

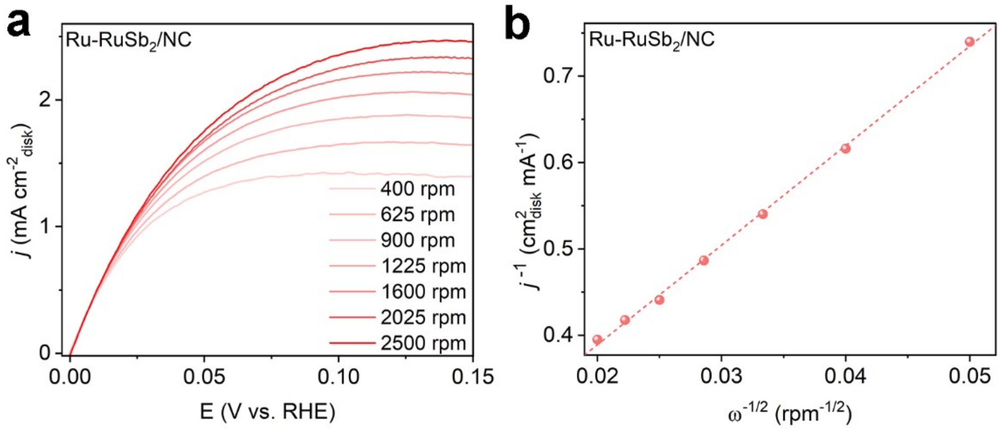

Figure S5 (a) Polarization curves of Ru-RuSb$_2$/NC in H_2-saturated 0.1 M KOH solution at the rotating speeds varied from 2500 to 400 rpm. (b) And the corresponding Koutecky–Levich plot.

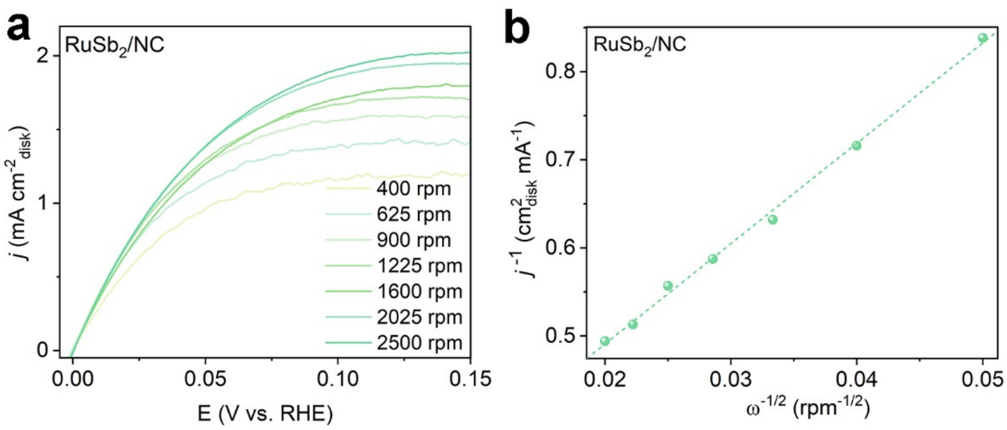

Figure S6 (a) Polarization curves of RuSb$_2$/NC in H_2-saturated 0.1 M KOH solution at the rotating speeds varied from 2500 to 400 rpm. (b) And the corresponding Koutecky–Levich plot.

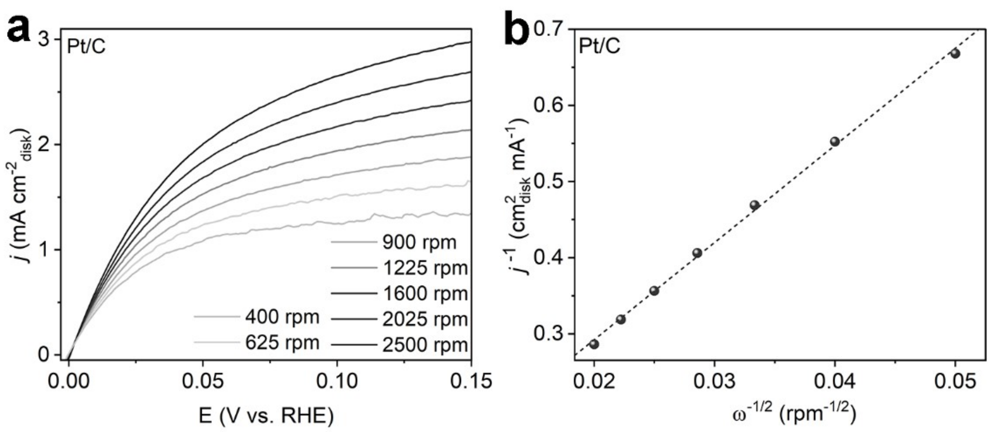

Figure S7 (a) Polarization curves of Pt/C_{com} in H_2-saturated 0.1 M KOH solution at the rotating speeds varied from 2500 to 400 rpm. (b) And the corresponding Koutecky–Levich plot.

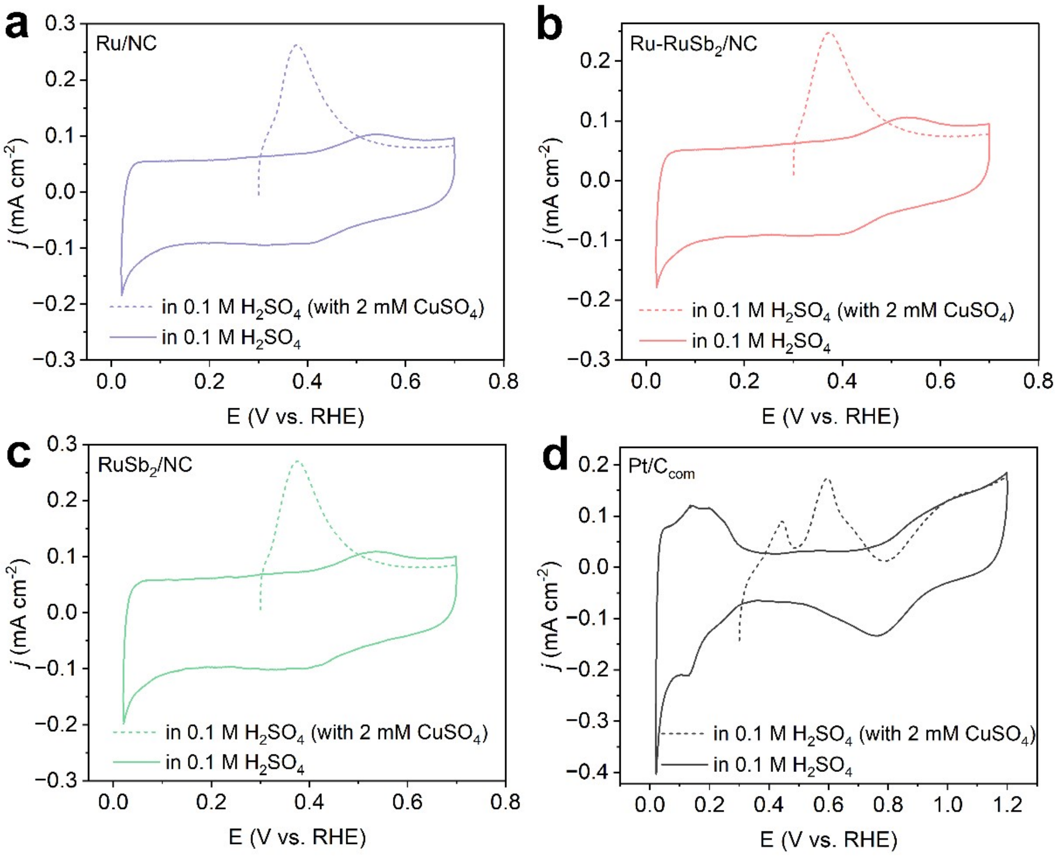

Figure S8 The CV curves of Ru/NC (a), Ru-RuSb$_2$/NC (b), RuSb$_2$/NC (C) and Pt/C$_{com}$ (d) as well as the Cu-UPD zones.

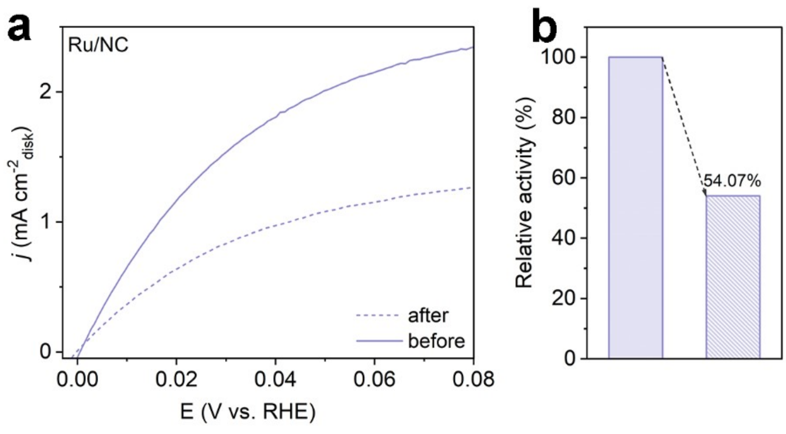

Figure S9 (a) polarization curves of Ru /NC in H$_2$-saturated 0.1 M KOH at a rotating speed of 1600 rpm before and after 1000 CV. (b) Comparation of the HOR performance after the stability test.

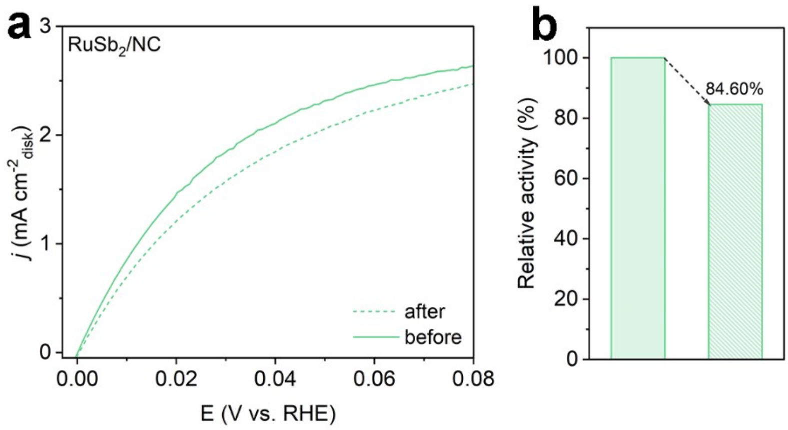

Figure S10 (a) polarization curves of $RuSb_2$/NC in H_2-saturated 0.1 M KOH at a rotating speed of 1600 rpm before and after 1000 CV. (b) Comparation of the HOR performance after the stability test.(改范围到 0.08)

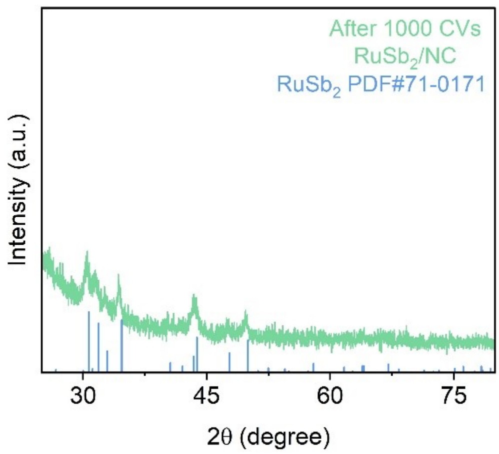

Figure S11 The XRD pattern of $RuSb_2$/NC after the stability test.

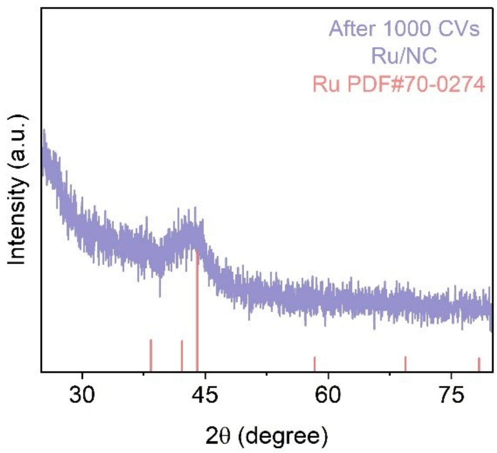

Figure S12 The XRD pattern of Ru/NC after the stability test.

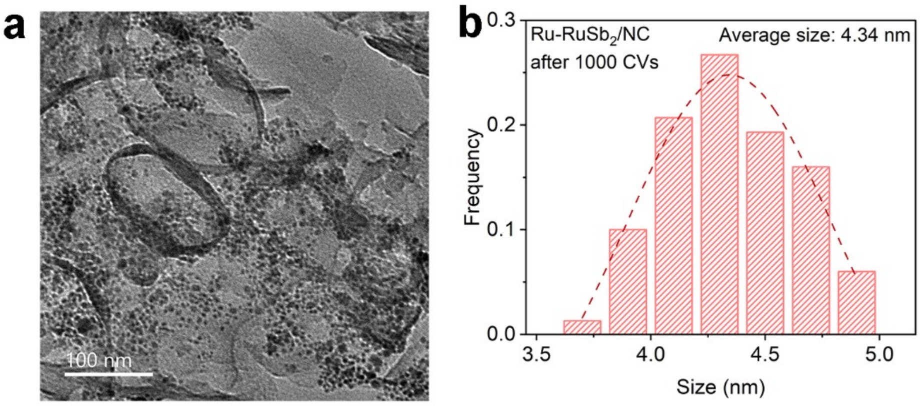

Figure S13 The TEM images of Ru-$RuSb_2$/NC (a) and the corresponding size distribution of (b) after the stability test.

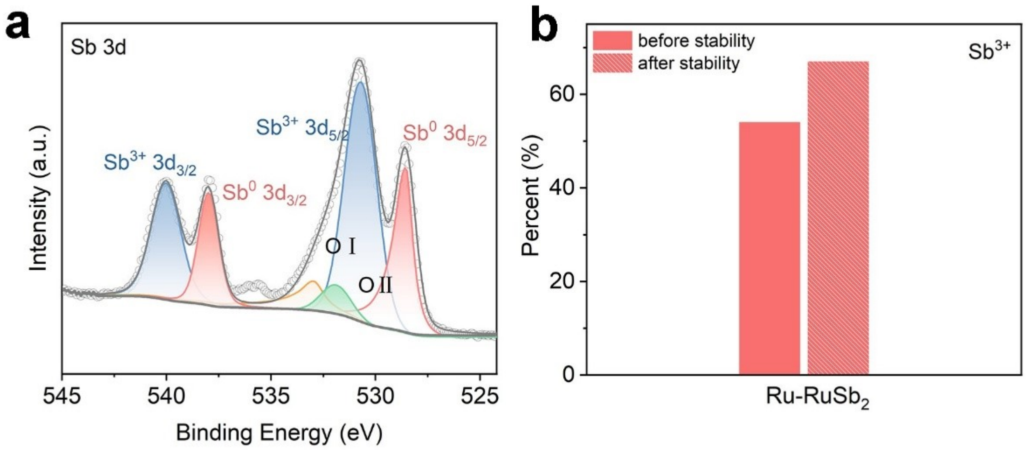

Figure S14 (a)The Sb 3d XPS spectra of Ru-$RuSb_2$/NC after the stability test. (b) The corresponding rations of Sb^{3+} in Ru-$RuSb_2$/NC before and after the stability test.

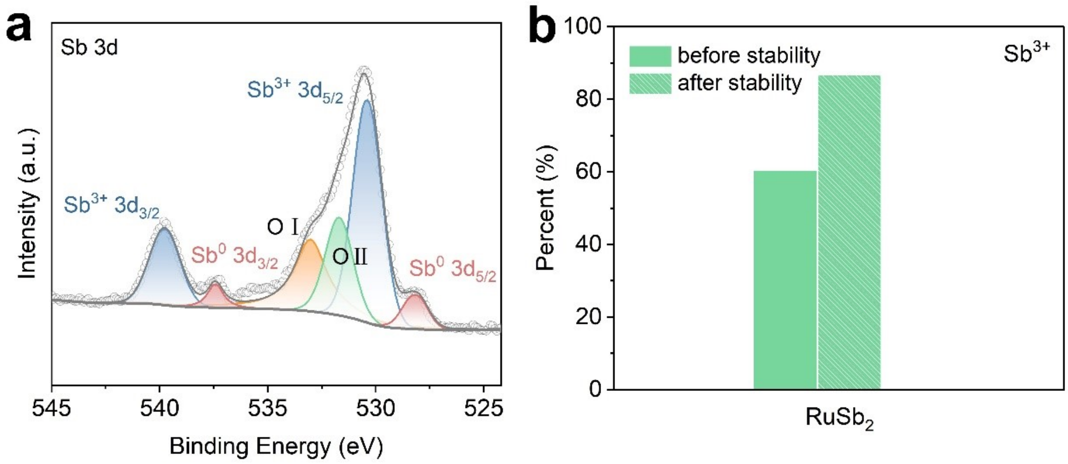

Figure S15 (a)The Sb 3d XPS spectra of $RuSb_2$/NC after the stability test. (b) The corresponding rations of Sb^{3+} in $RuSb_2$/NC before and after the stability test.

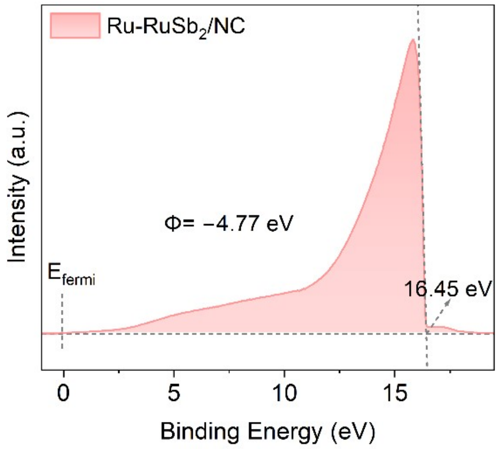

Figure S16 UPS spectra of the Ru-$RuSb_2$/NC.

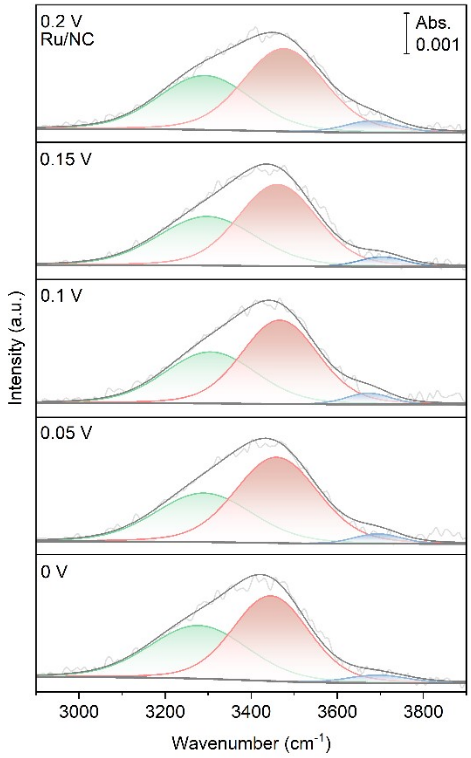

Figure S17 Deconvolution of the O-H stretching vibration features of in situ SEIRAS spectra recorded at potentials from 0 V to 0.2 V vs RHE for Ru/NC.

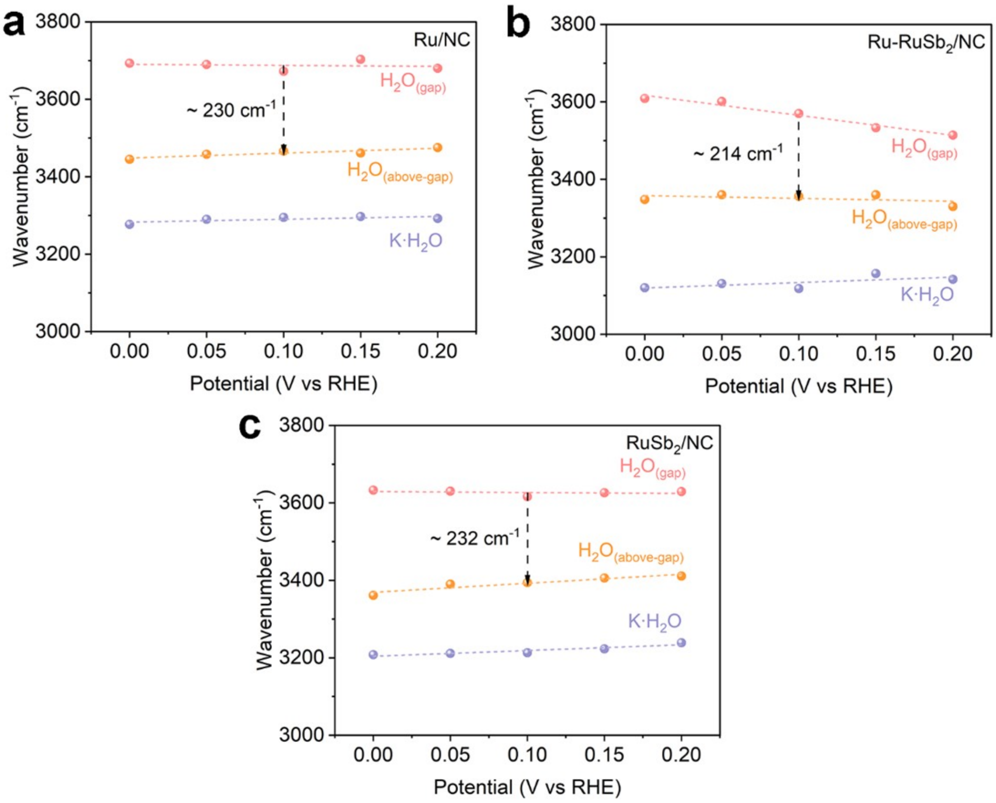

Figure S18 Changes of the O-H stretching vibration frequencies in SEIRAS spectra of various types of interfacial water of Ru/NC (a), Ru-RuSb$_2$/NC (b) and RuSb$_2$/NC (c).

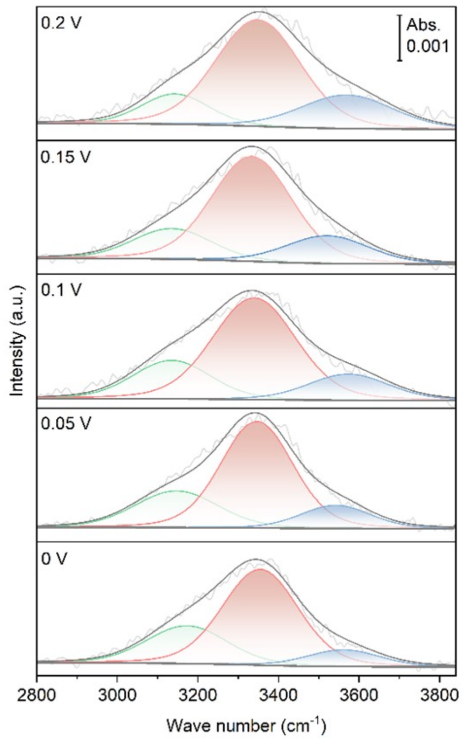

Figure S19 Deconvolution of the O-H stretching vibration features of in situ SEIRAS spectra recorded at potentials from 0 V to 0.2 V vs RHE for Ru-RuSb$_2$/NC after stability.

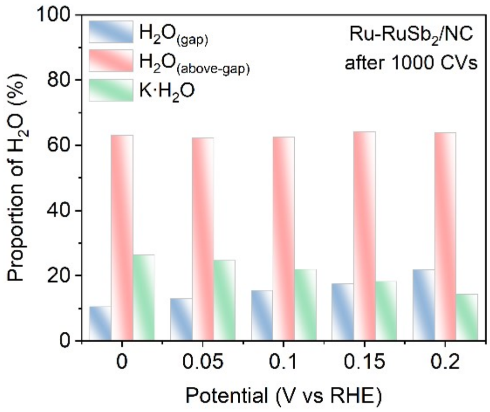

Figure S20 The proportion of the three kinds of water molecules from the deconvolution of the O-H stretching vibration features of Ru-RuSb$_2$/NC after stability.

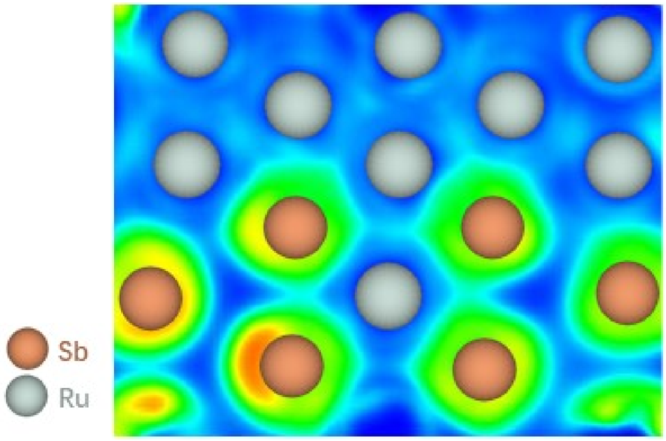

Figure S21 ELF of Ru-RuSb$_2$.

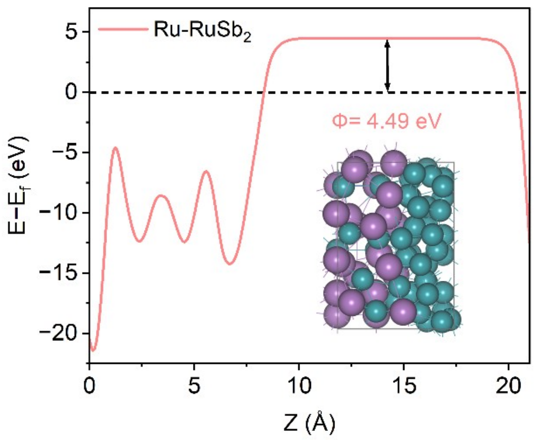

Figure S22 The electrostatic potential profiles of Ru-RuSb$_2$ surface, which is plotted relative to the corresponding Fermi levels. The insets is the corresponding structure models Ru-RuSb$_2$. The purple balls present Sb atoms and green balls present Ru atoms.

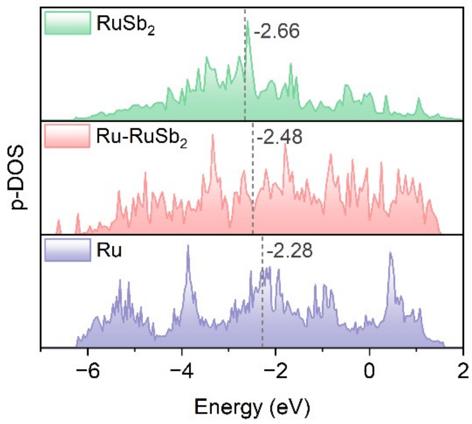

Figure S23 The projected density of states of Ru in Ru, Ru-$RuSb_2$ and $RuSb_2$.

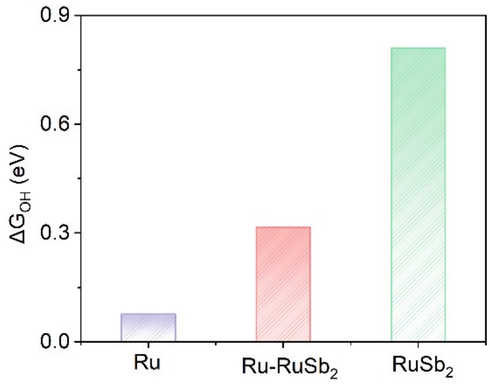

Figure S24 The adsorption energy of OH* on Ru sites in Ru, Ru-$RuSb_2$ and $RuSb_2$.

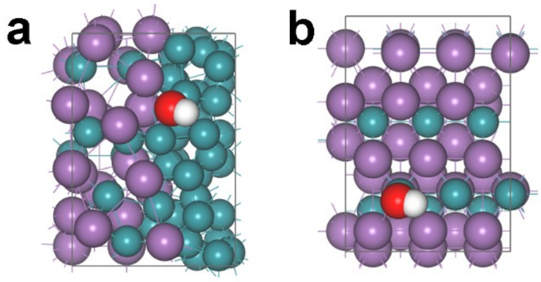

Figure S25 The optimal theoretical structures of OH* on Ru sites of Ru-$RuSb_2$(a) and $RuSb_2$(b). The purple balls present Sb atoms, green balls present Ru atoms, red balls present O atoms and white balls present H atoms.

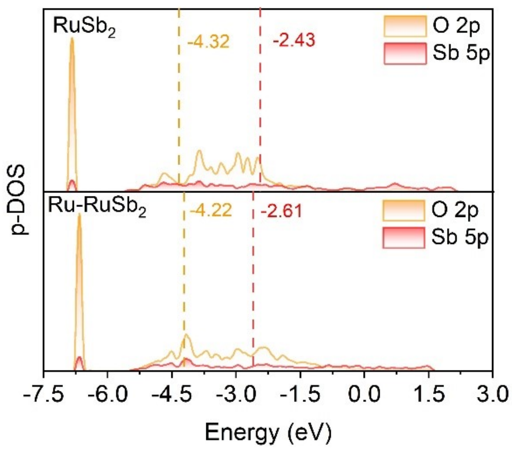

Figure S26 Energy band diagram of OH adsorption state of $RuSb_2$ (a) and Ru-$RuSb_2$ (b).

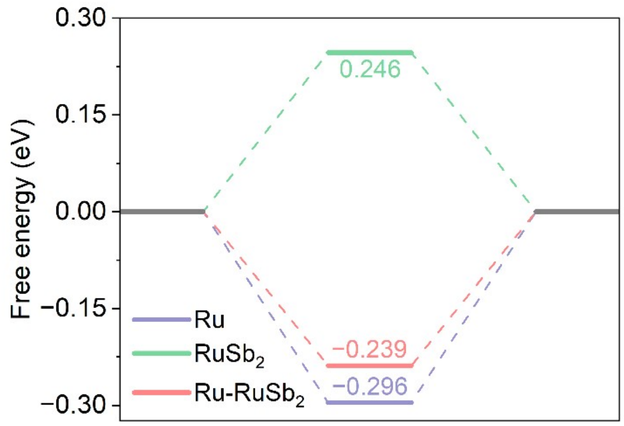

Figure S27 The adsorption energy of H* on Ru, Ru-$RuSb_2$ and $RuSb_2$.

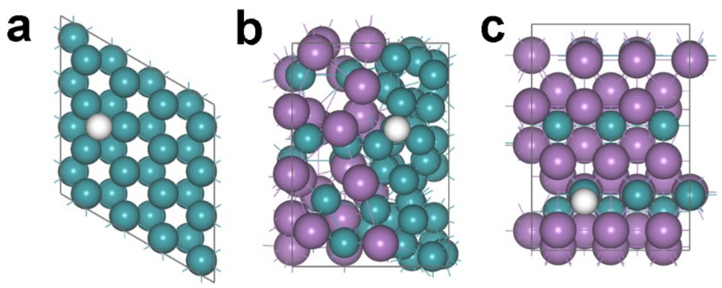

Figure S28 The optimal theoretical structures of H* on Ru sites of Ru(a) Ru-$RuSb_2$(b) and $RuSb_2$(c). The purple balls present Sb atoms, green balls present Ru atoms and white balls present H atoms.

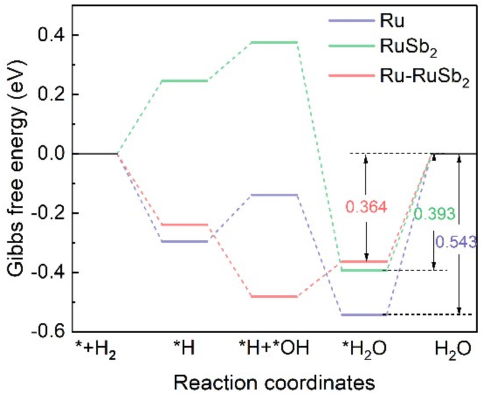

Figure S29 The reaction pathways of Ru, Ru-$RuSb_2$ and $RuSb_2$.

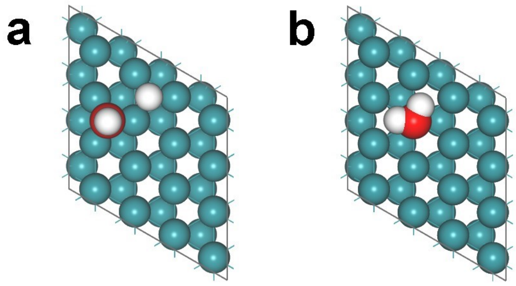

Figure S30 The optimal theoretical structures of H*+OH* (a) and H_2O (b) of Ru. The green balls present Ru atoms, white balls present H atoms and red balls present O atoms.

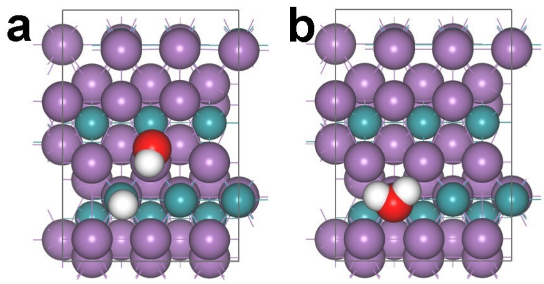

Figure S31 The optimal theoretical structures of H*+OH* (a) and H_2O (b) of $RuSb_2$. The purple balls present Sb atoms, green balls present Ru atoms, white balls present H atoms and red balls present O atoms.

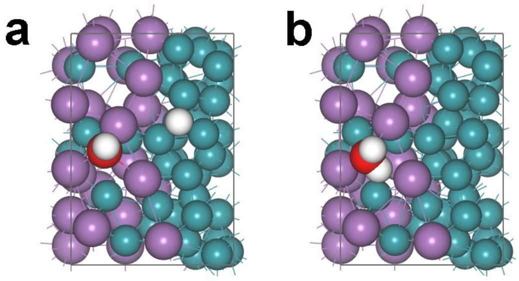

Figure S32 The optimal theoretical structures of H*+OH* (a) and H_2O (b) of Ru-$RuSb_2$. The purple balls present Sb atoms, green balls present Ru atoms, white balls present H atoms and red balls present O atoms.

Table S1 ICP-AES results of the contents of Ru and Sb in different catalysts.

Catalyst	Ru (wt. %)	Sb(wt. %)
$RuSb_2$	12.14	16.18
Ru-$RuSb_2$	10.85	12.50
Ru	17.96	/

Table S2. HOR activities of the reported PGM-based catalysts in alkaline media.

Catalyst	Loading (μg_{PGM} cm^{-2})	$j^{0,s}$ (mA cm_{metal}^{-2})	$j^{k,m}$@50 mV (mA μg_{metal}^{-1})	Reference
Ru-$RuSb_2$/NC	5.53	0.591	2.098	This work
PtRu/Mo_2C-TaC	13	0.2	0.291	[10]
$Ru_{0.7}Ni_{0.3}$/C	14	0.130	0.140	[11]
Ir-Ru@C	25.6	0.133	0.75	[12]
Ru-Ir(2/3)/C	10	0.283	0.210	[13]
D-Pt_3In	10	/	0.934	[14]
IO-Ru-TiO_2/C	25.48	0.109	0.907	[15]
Ru@TiO_2	230	/	~0.290	[16]
Ru-$Cr_1(OH)_x$-1.1	60	0.28	0.425	[17]

$Ir/\alpha\text{-}MoC_{1-x}$	/	0.455	0.445	[18]
Pt_3Ni NWs/C	15.3	0.31	0.77	[19]
$Rh@Pt_{0.83}$ NBs	10.2	0.590	0.214	[20]
$Ru\text{-}TiO/TiO_2@NC$	25.5	0.271	0.107	[21]
Pt-MoC@NC	10	0.560	0.833	[22]
Ru@NC/C-400	20.4	0.300	0.250	[23]
Rh NBs/C	6.25	0.146	0.321	[24]
PtRh NAA	25.5	0.340	0.322	[25]
$Pd_{0.33}Ir_{0.67}/N\text{-}C$	10	0.45	0.481	[26]
Ru Colloidosomes	~57	~0.045	~0.047	[27]
PtMo NPs/C	~9.43	0.63	0.805	[28]
$PtMo/MoO_{x-1}/C$	~9.43	0.83	3.19	[28]
PtRu-NWs	20	0.493	2.2	[29]
Ir_1Ru_3NWs/C	29	0.0838	3.346	[30]
E/O-PtFeCoNiMn/C	~16	0.705	0.466	[31]
Ru/PEI-XC	21.7	0.687	0.423	[32]
$B_{int}\text{-}Rh_{hcp}/C$	7.34	0.463	1.413	[33]
Ru_2P/C	6.45	0.389	0.877	[34]
B-Ru/C	7.49	0.316	1.716	[35]
Sn-Ru/C	6.26	0.470	1.790	[36]

References

1. Cong, Y. Y.; Yi, B. L.; Song, Y. J., Hydrogen oxidation reaction in alkaline media: From mechanism to recent electrocatalysts. *Nano Energy* **2018,** *44*, 288-303.
2. Sheng, W. C.; Gasteiger, H. A.; Shao-Horn, Y., Hydrogen Oxidation and Evolution Reaction Kinetics on Platinum: Acid vs Alkaline Electrolytes. *J. Electrochem. Soc.* **2010,** *157* (11), B1529-B1536.

3. Zheng, J.; Zhuang, Z. B.; Xu, B. J.; Yan, Y. S., Correlating Hydrogen Oxidation/Evolution Reaction Activity with the Minority Weak Hydrogen-Binding Sites on Ir/C Catalysts. *ACS Catal.* **2015,** *5* (7), 4449-4455.
4. Durst, J.; Siebel, A.; Simon, C.; Hasché, F.; Herranz, J.; Gasteiger, H. A., New insights into the electrochemical hydrogen oxidation and evolution reaction mechanism. *Energy Environ. Sci.* **2014,** *7* (7), 2255-2260.
5. Ohyama, J.; Sato, T.; Yamamoto, Y.; Arai, S.; Satsuma, A., Size Specifically High Activity of Ru Nanoparticles for Hydrogen Oxidation Reaction in Alkaline Electrolyte. *J Am Chem Soc*, **2013**, *135*, 8016-8021.
6. Duan, Y.; Yu, Z. Y.; Yang, L.; Zheng, L. R.; Zhang, C. T.; Yang, X. T.; Gao, F. Y.; Zhang, X. L.; Yu, X. X.; Liu, R.; Ding, H. H.; Gu, C.; Zheng, X. S.; Shi, L.; Jiang, J.; Zhu, J. F.; Gao, M. R.; Yu, S. H., Bimetallic nickel-molybdenum/tungsten nanoalloys for high-efficiency hydrogen oxidation catalysis in alkaline electrolytes. *Nat. Commun.* **2020,** *11* (1), 4789.
7. Perdew, J. P.; Burke, K.; Ernzerhof, M., Generalized gradient approximation made simple (vol 77, pg 3865, 1996). *Phys. Rev. Lett.* **1997,** *78* (7), 1396-1396.
8. Hammer, B.; Hansen, L. B.; Norskov, J. K., Improved adsorption energetics within density-functional theory using revised Perdew-Burke-Ernzerhof functionals. *Phys. Rev. B* **1999,** *59* (11), 7413-7421.
9. Norskov, J. K.; Bligaard, T.; Logadottir, A.; Kitchin, J. R.; Chen, J. G.; Pandelov, S.; Norskov, J. K., Trends in the exchange current for hydrogen evolution. *J. Electrochem. Soc.* **2005,** *152* (3), J23-J26.
10. Hamo, E. R.; Singh, R. K.; Douglin, J. C.; Chen, S.; Hassine, M. B.; Carbo-Argibay, E.; Lu, S.; Wang, H.; Ferreira, P. J.; Rosen, B. A.; Dekel, D. R., Carbide-Supported PtRu Catalysts for Hydrogen Oxidation Reaction in Alkaline Electrolyte. *ACS Catal* **2021**, 11 (2), 932-947.
11. Wang, H.; Yang, Y.; DiSalvo, F. J.; Abruña, H. D., Multifunctional Electrocatalysts: Ru–M (M = Co, Ni, Fe) for Alkaline Fuel Cells and Electrolyzers. *ACS Catal* **2020**, 10 (8), 4608-4616.
12. Huang, M.; Yang, H.; Xia, X.; Peng, C., Highly active and robust Ir-Ru electrocatalyst for alkaline HER/HOR: Combined electronic and oxophilic effect. *Appl. Catal. B Environ. Energy* **2024**, 358, 124422.
13. Ishikawa, K.; Ohyama, J.; Okubo, K.; Murata, K.; Satsuma, A., Enhancement of Alkaline Hydrogen Oxidation Reaction of Ru–Ir Alloy Nanoparticles through Bifunctional Mechanism on Ru–Ir Pair Site. *ACS Appl Mater. Interfaces* **2020**, 12 (20), 22771-22777.
14. Wu, J.; Gao, X.; Liu, G.; Qiu, X.; Xia, Q.; Wang, X.; Zhu, W.; He, T.; Zhou, Y.; Feng, K.; Wang, J.; Huang, H.; Liu, Y.; Shao, M.; Kang, Z.; Zhang, X., Immobilizing Ordered Oxophilic Indium Sites on Platinum Enabling Efficient Hydrogen Oxidation in Alkaline Electrolyte. *J. Am. Chem. Soc.* **2024**, 146 (29), 20323-20332.
15. Jiang, J.; Tao, S.; He, Q.; Wang, J.; Zhou, Y.; Xie, Z.; Ding, W.; Wei, Z., Interphase-oxidized ruthenium metal with half-filled d-orbitals for hydrogen oxidation in an alkaline solution. *J. Mater. Chem.* A **2020**, 8 (20), 10168-10174.
16. Zhou, Y.; Xie, Z.; Jiang, J.; Wang, J.; Song, X.; He, Q.; Ding, W.; Wei, Z., Lattice-confined Ru clusters with high CO tolerance and activity for the hydrogen oxidation reaction. *Nat. Catal.* **2020**, 3 (5), 454-462.
17. Zhang, B.; Zhang, B.; Zhao, G.; Wang, J.; Liu, D.; Chen, Y.; Xia, L.; Gao, M.; Liu, Y.; Sun, W.; Pan, H., Atomically dispersed chromium coordinated with hydroxyl clusters enabling efficient hydrogen oxidation on ruthenium. *Nat. Commun.* **2022**, 13 (1), 5894.
18. Han, Y.; Zhao, L.; Cheng, W.; Wang, M.; Yang, L.; Lin, Y.; Xu, K., Iridium Cluster Anchored onto Cubic Molybdenum Carbide with Strong Electronic Interactions for Robust Hydrogen Oxidation

Reaction in Alkaline Medium. *Adv. Funct. Mater.* **2024**, 34 (44), 2407060.

19. Wang, L.; Meng, S.; Tang, C.; Zhan, C.; Geng, S.; Jiang, K.; Huang, X.; Bu, L., PtNi/PtIn-Skin Fishbone-Like Nanowires Boost Alkaline Hydrogen Oxidation Catalysis. *ACS Nano* **2023,** *17* (18), 17779-17789.
20. Cai, J.; Liao, X.; Li, P.; Wang, Q.; Huang, H.; Lyu, Z.; Lin, J.; Xie, S., Penta-Twinned Rh@Pt Core-Shell nanobranches with engineered shell thickness for reversible and active hydrogen redox electrocatalysis. *Chem. Eng. J.* **2022**, 429, 132414.
21. Jing, L.; Jie, G.; Yu, W.; Ren, H.; Cui, X.; Chen, X.; Jiang, L., A unique sandwich-structured Ru-TiO/TiO_2@NC as an efficient bi-functional catalyst for hydrogen oxidation and hydrogen evolution reactions. *Chem. Eng. J.* **2023**, 472, 145009.
22. Zhou, F.; Ke, X.; Chen, Y.; Zhao, M.; Yang, Y.; Dong, Y.; Zou, C.; Chen, X. a.; Jin, H.; Zhang, L.; Wang, S., Electron-distribution control via Pt/NC and MoC/NC dual junction: Boosted hydrogen electro-oxidation and theoretical study. *J. Energy Chem.* **2024**, 88, 513-520.
23. Liu, J.; Zhang, B.; Fo, Y.; Gao, J.; Yu, W.; Ren, H.; Cui, X.; Zhou, X.; Jiang, L., Unique Ru nanoclusters confined in carbon molecular sieve coatings with tailoring sub-4Å ultramicropores as a highly efficient and CO-tolerant hydrogen oxidation electrocatalyst. *Chem. Eng. J.* **2023**, 468, 143438.
24. Zhang, Y.; Li, G.; Zhao, Z.; Han, L.; Feng, Y.; Liu, S.; Xu, B.; Liao, H.; Lu, G.; Xin, H. L.; Huang, X., Atomically Isolated Rh Sites within Highly Branched Rh_2Sb Nanostructures Enhance Bifunctional Hydrogen Electrocatalysis. *Adv. Mater.* **2021**, 33 (43), 2105049.
25. Jin, Y.; Chen, F.; Wang, J.; Guo, L.; Jin, T.; Liu, H., Lamellar platinum–rhodium aerogels with superior electrocatalytic performance for both hydrogen oxidation and evolution reaction in alkaline environment. *J. Power Sources* **2019**, 435, 226798.
26. Cong, Y.; McCrum, I. T.; Gao, X.; Lv, Y.; Miao, S.; Shao, Z.; Yi, B.; Yu, H.; Janik, M. J.; Song, Y., Uniform $Pd_{0.33}Ir_{0.67}$ nanoparticles supported on nitrogen-doped carbon with remarkable activity toward the alkaline hydrogen oxidation reaction. *J. Mater. Chem.* A **2019**, 7 (7), 3161-3169.
27. Yang, X.; Ouyang, B.; Shen, P.; Sun, Y.; Yang, Y.; Gao, Y.; Kan, E.; Li, C.; Xu, K.; Xie, Y., Ru Colloidosome Catalysts for the Hydrogen Oxidation Reaction in Alkaline Media. *J. Am. Chem. Soc.* **2022**, 144 (25), 11138-11147.
28. Luo, H.; Wang, K.; Lin, F.; Lv, F.; Zhou, J.; Zhang, W.; Wang, D.; Zhang, W.; Zhang, Q.; Gu, L.; Luo, M, and Guo, S. Amorphous MoO with High Oxophilicity Interfaced with PtMo Alloy Nanoparticles Boosts Anti-CO Hydrogen Electrocatalysis. *Adv. Mater.* **2023**, 35, 2211854.
29. Wang, Y.; Wang, G. W.; Li, G. W.; Huang, B.; Pan, J.; Liu, Q.; Han, J. J.; Xiao, L.; Lu, J. T.; Zhuang, L., Pt-Ru catalyzed hydrogen oxidation in alkaline media: oxophilic effect or electronic effect? *Energy Environ. Sci.* **2015**, 8 (1), 177-181.
30. Qin, B. W.; Yu, H. M.; Gao, X. Q.; Yao, D. W.; Sun, X. Y.; Song, W.; Yi, B. L.; Shao, Z. G., Ultrathin IrRu nanowire networks with high performance and durability for the hydrogen oxidation reaction in alkaline anion exchange membrane fuel cells. *J. Mater. Chem. A* **2018**, 6 (41), 20374-20382.
31. Huang, Z.; Peng, Y.; Xing, L.; Xu, M.; Fang, M.; Xie, H.; Li, J.; Zhou, Y.; Wu, P.; Wang, N.; Tang, C.; Wu, M.; Wang, L.; Ye, S, and Du, L. Microenvironment regulation to synthesize sub-3 nm Pt-based high-entropy alloy nanoparticles enabling compressed lattice to boost electrocatalysis. *Appl. Catal., B* **2025**, 363, 124775.
32. Wang, J.; Liu, J.; Zhang, B. Y.; Gao, J.; Liu, G. B.; Cui, X. J.; Liu, J. X.; Jiang, L. H., Amine-ligand modulated ruthenium nanoclusters as a superior bi-functional hydrogen electrocatalyst in alkaline media. *J. Mater. Chem. A* **2021**, 9 (40), 22934-22942.
33. Han, P.; Wu, L.; Zhang, Y.; Yue, J.; Jin, Y.; Jia, H, and Luo, W. An Interstitial Boron Inserted

Metastable Hexagonal Rh Nanocrystal for Efficient Hydrogen Oxidation Electrocatalysis. *Angew. Chem. Int. Ed.* **2025**, 64, e202419320.

34. Jin, Y.; Fan, X.; Cheng, W.; Zhou, Y.; Xiao, L, and Luo, W. The Role of Phosphorus on Alkaline Hydrogen Oxidation Electrocatalysis for Ruthenium Phosphides. *Angew. Chem. Int. Ed.* **2024**, 63, e202406888.
35. Han, P.; Yang, X.; Wu, L.; Jia, H.; Chen, J.; Shi, W.; Cheng, G, and Luo, W. A Highly-Efficient Boron Interstitially Inserted Ru Anode Catalyst for Anion Exchange Membrane Fuel Cells. *Adv. Mater.* **2024**, 36, 2304496.
36. Wu, L.; Su, L.; Liang, Q.; Zhang, W.; Men, Y, and Luo, W. Boosting Hydrogen Oxidation Kinetics by Promoting Interfacial Water Adsorption on d-p Hybridized Ru Catalysts. *ACS Catal.* **2023**, 13, 4127-4133.